Multivariable Coordinated Control Strategy for Efficiency Optimization Without Real-Time Wireless Feedback Communication in Wireless Power Transfer

JIANTING LI [ID], (Member, IEEE), JINQUAN WANG, JIANKE LI [ID], AND JINGJING CHEN
National Defense Engineering College, Army Engineering University of PLA, Nanjing 210007, China
Corresponding author: Jianke Li (511746569@qq.com)

ABSTRACT This paper presents a constant-frequency multi-variable coordinated control strategy based on a series-series compensated dual-active-bridge wireless-power-transfer converter to eliminate real-time wireless feedback communication (RTWFC) and optimize efficiency. The use of switch-controlled capacitors as the primary and secondary resonant capacitors allows the continuous change of the compensation capacitance for the inverter soft-switching and reactance matching, respectively. The output voltage is regulated by tuning the phase-shift angle in the active rectifier bridge. The optimal load resistance for efficiency improvement is matched by adjusting the phase difference between the rectifier voltage and current based on the load and mutual inductance estimation. Moreover, the phase shift of the inverter, which is load-independent, and the coupling coefficient between the coils are positively correlated. Nevertheless, the drawbacks of the proposed control strategy are that optimal load matching is only valid for heavy load and constant current cannot be realized while keeping the constraint of the decoupled control. The proposed control strategy is experimentally validated on a prototype. The efficiency improvement is 5% compared to the conventional voltage tuning with a diode rectifier at the rated output power and in the normal position, and the peak efficiency reaches 93.6% at a 24 V output under the coupling coefficient of 0.3. In addition, a faster transient response was demonstrated in the proposed control strategy without RTWFC for output regulation.

INDEX TERMS Wireless power transfer, soft switching, control strategy, efficiency optimization, switch-controlled capacitor.

I. INTRODUCTION

Wireless power transfer (WPT) has attracted increasing attention in power electronics research. Millions of wireless chargers are powering smartphones worldwide. Since the WPT system features no physical contact, safety, and convenience, numerous studies have focused on the application of automatic guided vehicles (AGVs), robotics, unmanned aerial vehicles (UAVs), and electric vehicles (EVs) [1].

The constant current (CC) or constant voltage (CV) output is preferred in different applications. Various methods, such as the frequency tuning [2]–[7], multi-stage via extra DC/DC converter [8]–[10], higher-order compensation network [11]–[13], hybrid compensation networks [14], and capacitor or inductor tuning [15]–[23], have been studied to

The associate editor coordinating the review of this manuscript and approving it for publication was Vitor Monteiro [ID].

modulate the output of WPT systems. Voltage and frequency tuning are the two main methods for controlling the output under various coupling coefficients and load conditions [3]. In addition to the basic function of the output regulation, the power transfer efficiency is another key factor in a power electronics system. Zero-voltage-switching (ZVS) on the inverter switches and zero-phase-angle (ZPA) between the inverter output voltage and current have been studied in [7], [9], [15] to improve the efficiency. Besides, various impedance matching methods have been used to compensate for the variation in resonant elements from the misalignment of coils, environmental effects, ambient temperature, load conditions, aging, etc. [15]–[23]. The continuously tuned capacitance using the switch-controlled capacitor (SCC) was implemented on the series-series (SS) compensation network in [15], [16], [22], [23] and Inductor-Capacitor-Capacitor-Series (LCC-S) compensation network in [17], [18] to tune

TABLE 1. Comparison to the literature.

Reference	Compensation	No extra DC/DC	Active rectifier	CC&CV output	Inverter soft switching	No wireless feedback communication	Optimal load matching		Reactance compensation
							Narrow range	Wide range	
[4]	SS	√	√	×	√	×	√	√	×
[5]	SS	√	√	√	√	√	×	×	×
[23]	SS	√	√	×	√	×	√	√	√
[24][25]	SS	×	×	×	√	√	×	×	×
[26]	LCC-LCC	×	√	×	√	√	×	×	×
[27][28][32]	SS	√	√	×	√	√	×	×	×
[29][30]	SS	√	×	√	√	√	×	×	×
[31]	SS	√	×	√	×	√	×	×	×
This study	SS	√	√	×	√	√	√	×	√

the impedance. The efficiency varies with the equivalent load resistance, and there is an optimal load resistance to achieve higher efficiency. Thus, the phase shift of the active rectifier is adjusted to match the optimal load in [23] to improve efficiency.

Nevertheless, all the above solutions rely on real-time wireless feedback communication (RTWFC) for the output regulation. The long propagation delay in wireless communication can result in control stability and reliability issues. A dual-side control based on the LCC-SP compensation network was proposed in [8] to regulate the output current and voltage by modulating the secondary extra DC/DC converter. Both the CC and CV outputs with the ZPA of the inverter were realized on a series-parallel series (S-PS) compensation network without feedback communication [9]. However, the inverter input voltage should be adjusted to deliver the rated power with the CV mode, indicating that an extra DC/DC stage is required to modulate the inverter input voltage. An extra DC/DC stage was employed for the primary-side control in [24] and secondary-side control in [25], to eliminate wireless feedback communication. However, the extra DC/DC stage deteriorates the power density and adds additional costs and power losses. An active rectifier was implemented in [26]–[28] to regulate the output voltage without wireless feedback communication to the primary side. Various control methods were studied in [29]–[31] to regulate the output in a single-stage converter with a passive rectifier without RTWFC. Nevertheless, neither the optimal load matching nor the impedance compensation has been realized to improve the power transfer efficiency.

To address the aforementioned drawbacks, this study proposes a control strategy based on an SS compensation network and a dual-active-bridge (DAB) converter to provide a CV source. A comparison of the key features between this study and previous publications is presented in Table 1. Multivariable are coordinately controlled to achieve a CV output over various load conditions and magnetic couplings with efficiency optimization. Therefore, the proposed control strategy cannot accomplish a CC output while keeping the constraints of the decoupled control and efficiency optimization. In addition, the optimal load matching helps to enhance the efficiency in heavy load conditions, although it turns to be invalid in light load conditions due to the limitation of phase-shift regulation. The proposed system is suitable for a variety of applications, such as the power supplies
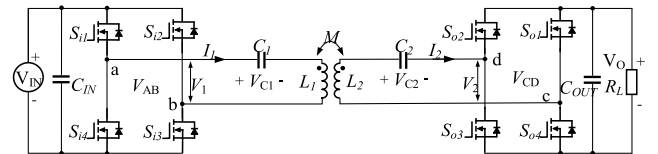

FIGURE 1. Circuit of DAB converter with SS compensation network.

for cleanroom equipment and rotating equipment without a wire connection. The main contributions of this study are as follows:

1) This paper proposes a novel multi-variable coordinated control strategy for the SS compensated WPT system. Both efficiency optimization and decoupled control without RTWFC are realized to achieve a CV output over various load conditions and magnetic couplings in a single-stage converter.

2) The inverter phase shift is constant for different load conditions and is adjusted to adapt to various magnetic coupling conditions. The SCCs are adopted in both the primary and secondary resonant capacitors for soft switching and impedance tuning, respectively.

3) A unique relationship among multi variables on the secondary side, such as the phase shift of the active rectifier, the phase difference between the active rectifier voltage and current, and the phase of the secondary SCC, is established to realize the output regulation, as well as the optimal load matching in heavy load conditions and reactance compensation over various magnetic coupling conditions for efficiency optimization.

The remainder of this paper is organized as follows. Section II reviews the basic SS compensation topology and presents the proposed constant-frequency multivariable-coordinated control strategy. The implementation of the proposed control strategy is described in Section III. The theoretical analysis is verified on a prototype, and the measurement results are presented and discussed in section IV. Section V concludes the paper.

II. PROPOSED CONTROL STRATEGY BASED ON SS COMPENSATION TOPOLOGY
A. DAB CONVERTER WITH SS COMPENSATION NETWORK
The system schematic of the DAB converter with the SS compensation network is shown in Fig. 1, which contains the input voltage source V_{IN}, input filter capacitor C_{IN}, full-bridge
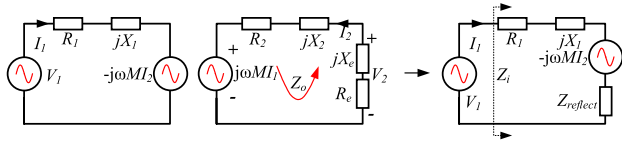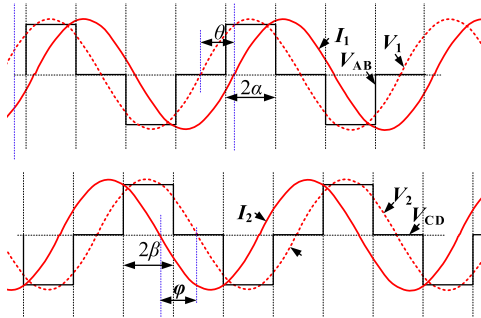
FIGURE 2. Equivalent circuits.

FIGURE 3. Definition of different phase angles.

inverter, a series resonant capacitor on the transmitter side C_1, transmitter coil L_1, receiver coil L_2, a series resonant capacitor on the receiver side C_2, full-bridge active rectifier, output filter capacitor C_{OUT}, and output load resistor R_L. k is the coupling coefficient between the transmitter and the receiver coils and varies according to the relative position between the transmitter coil and the receiver coil.

$$k = \frac{M}{\sqrt{L_1 L_2}} \tag{1}$$

where M is the mutual inductance between transmitter coil L_1 and receiver coil L_2. The resonant frequency ω_r of the transmitter coil and primary resonant capacitor is set to be the same as those of the receiver coil and secondary resonant capacitor to boost the power transfer capability.

$$\omega_r = 2\pi f_r = \frac{1}{\sqrt{L_1 C_1}} = \frac{1}{\sqrt{L_2 C_2}} \tag{2}$$

An equivalent circuit of the schematic of the system is shown in Fig. 2. The inverter output voltage $\mathbf{V}_{AB}$ is simplified to $\mathbf{V}_1$ based on fundamental harmonic approximation (FHA).

$$V_1 = \frac{2\sqrt{2}}{\pi} V_{IN} \sin(\alpha) \tag{3}$$

where 2α is the phase shift angle of the full-bridge inverter. Different phase angles in the inverter and rectifier are indicated in Fig. 3. The full-bridge receiver impedance Z_e, including the load resistance R_L, is expressed as:

$$Z_e = R_e + jX_e \tag{4}$$

$$R_e = \frac{8}{\pi^2} R_L \cos^2(\varphi) \sin^2(\beta) \tag{5}$$

$$X_e = \frac{4}{\pi^2} R_L \sin(2\varphi) \sin^2(\beta) \tag{6}$$

where 2β is the rectifier phase-shift angle and φ is the phase difference between the rectifier voltage and current.

$$\varphi = atan\left(\frac{X_e}{R_e}\right). \tag{7}$$

By solving R_e and X_e, the solution of β is resolved,

$$\beta = asin\left(\sqrt{\frac{\pi^2}{8} \frac{R_e^2 + X_e^2}{R_e \cdot R_L}}\right). \tag{8}$$

The impedances of the transmitter resonant *LC* network and the receiver resonant *LC* network are

$$Z_1 = R_1 + jX_1 \tag{9}$$

$$Z_2 = R_2 + jX_2, \tag{10}$$

where R_1 is the equivalent resistance of the transmitter coil and resonant capacitor, R_2 is the equivalent resistance of the receiver coil and resonant capacitor, and

$$X_1 = \omega_s L_1 - \frac{1}{\omega_s C_1} \tag{11}$$

$$X_2 = \omega_s L_2 - \frac{1}{\omega_s C_2}. \tag{12}$$

Therefore, the receiver network impedance can be derived,

$$Z_{out} = R_{out} + jX_{out} = R_2 + R_e + j(X_2 + X_e). \tag{13}$$

When reflecting the receiver network impedance to the transmitter side in Fig. 2, the reflected impedance can be derived according to reflection theory:

$$Z_{reflect} = \frac{(\omega_S M)^2}{Z_{out}}. \tag{14}$$

The input impedance seen by the inverter is

$$Z_{in} = R_{in} + jX_{in} = Z_1 + Z_{reflect}. \tag{15}$$

The phase difference θ between the inverter voltage $\mathbf{V}_{AB}$ and inverter current $\mathbf{I}_1$ can be expressed as

$$\theta = arctan\left(\frac{X_{in}}{R_{in}}\right). \tag{16}$$

Based on Kirchhoff's voltage law, the voltage equation in Fig. 2 can be derived as

$$\begin{bmatrix} Z_1 & j\omega_s M \\ j\omega_s M & Z_{out} \end{bmatrix} \begin{bmatrix} \mathbf{I_1} \\ -\mathbf{I_2} \end{bmatrix} = \begin{bmatrix} \mathbf{V_1} \\ 0 \end{bmatrix} \tag{17}$$

where $\mathbf{I_1}$ is the current of the transmitter coil, and $\mathbf{I_2}$ is the current of the receiver coil, both can be derived by solving (17) as follows:

$$\mathbf{I_1} = \frac{\mathbf{V_1}(R_2 + R_e + j(X_e + X_2))}{(\omega_S M)^2 + (R_1 + jX_1)(R_2 + R_e + j(X_e + X_2))} \tag{18}$$

$$\mathbf{I_2} = \frac{j\omega_S M \mathbf{V_1}}{(\omega_S M)^2 + (R_1 + jX_1)(R_2 + R_e + j(X_e + X_2))}. \tag{19}$$

The power transfer efficiency can be expressed as,

$$\eta = \frac{I_2^2 * R_e}{Re(\mathbf{V_1 I_1}^*)} \tag{20}$$

which can be simplified as,

$$\eta = \frac{(\omega_S M)^2 R_e}{(\omega_S M)^2 (R_2 + R_e) + R_1 \left((R_2 + R_e)^2 + (X_e + X_2)^2\right)}. \tag{21}$$

The following conditions, derived by solving the derivatives of X_2 and R_e, respectively, should be met to maximize the power transfer efficiency:

$$X_2 + X_e = 0 \tag{22}$$

$$R_{eOPT} = \sqrt{(\omega_S M)^2 \frac{R_2}{R_1} + R_2^2}. \tag{23}$$

The rectified output voltage V_O is

$$V_O = V_2 \frac{\pi}{2\sqrt{2} \, e^{j\varphi} \sin(\beta)}. \tag{24}$$

B. PROPOSED CONTROL STRATEGY

The proposed control strategy aims to eliminate RTWFC in the feedback control loop during the power transfer. Conventionally, the output voltage is measured and sent to a primary controller via real-time wireless communication for output regulation. Instead, an active rectifier is utilized to regulate the output in the receiver, and the control in the transmitter and receiver is decoupled. Besides, the phase difference between the rectifier voltage and current is adapted for optimal load matching, and dynamic capacitance tuning is implemented for reactance compensation in the resonant networks of both transmitter and receiver. However, wireless communication is adapted to exchange information between the transmitter and receiver for initialization, where the propagation delay from wireless communication is much less critical than feedback control in the power transfer state.

According to (24), the phase angle β can be used to regulate the output voltage, because both β and φ contribute to R_e according to (5), and (23) limits the optimal equivalent load resistance, and the optimal phase angle φ for maximized efficiency can be solved by solving (5), (6), and (23):

$$\varphi = atan\left(X_e \sqrt{\frac{R_1}{R_2 \left((\omega_S M)^2 + R_1 \cdot R_2\right)}}\right). \tag{25}$$

Hence, both β and φ are fixed for proper output voltage and optimal efficiency, respectively. To fulfill the constraint in (22) for efficient power transfer, X_2 should be adjustable to match the rectifier network impedance.

The output power is calculated as follows,

$$P_{out} = I_2^2 R_e. \tag{26}$$

Substituting (19) and (23) into (26) and assuming $R_1 = 0$ and $R_2 = 0$,

$$P_{out} = \frac{8}{\pi^2} \frac{\omega_S M V_{IN}^2 \sin^2(\alpha)}{(\omega_S M)^2 + X1^2}. \tag{27}$$

On the transmitter side, the phase ε between the rising edge of the inverter output voltage $\mathbf{V}_{AB}$ and inverter current $\mathbf{I}_1$ is expressed as

$$\varepsilon = \theta - \frac{\pi}{2} + \alpha. \tag{28}$$

The inverter current $\mathbf{I}_1$ should lag the rising edge of the inverter output voltage $\mathbf{V}_{AB}$ for soft-switching of the inverter switches. In other words, the phase difference ε should be positive (i.e., $\varepsilon \geq 0$) to maintain ZVS. Therefore,

$$\alpha = \frac{\pi}{2} - \theta. \tag{29}$$

The phase-shift 2α of the full-bridge inverter meets the following constraints,

$$0 \leq 2\alpha \leq \pi. \tag{30}$$

By combining (16), (27), and (29) into (30), the constraints on the mutual inductance M are derived as follows:

$$M \leq \frac{8}{\pi^2} \frac{V_{IN^2}}{\omega_S P_{out}}. \tag{31}$$

It is assumed M_{max} is the maximum mutual inductance, which is defined at the specified input voltage and rated output power, and k_{max} is the maximum possible coupling coefficient. Thus, although the positions between the transmitter and receiver coils might vary, both M_{max} and the maximum coupling coefficient k_{max} are unique for a given system. The ratio x is defined as follows:

$$x = \frac{M}{M_{max}} = \frac{k}{k_{max}} \tag{32}$$

$$M_{max} = \frac{8}{\pi^2} \frac{V_{IN^2}}{\omega_S P_{out.rated}}. \tag{33}$$

By solving (16), (27), and (29), the relationship between α and k is derived and plotted in Fig. 4.

$$\alpha = \frac{\pi}{2} - atan\left(\sqrt{\sqrt{\left(\frac{k}{k_{max}}\right)^{-1}} - 1}\right). \tag{34}$$

As shown in (34) and Fig. 4, a specific coupling coefficient corresponds to a specific inverter phase-shift angle 2α, and the inverter phase shift is independent of the load conditions. Therefore, the inverter phase shift 2α and the coupling coefficient k between the coils are positively correlated, and the inverter phase shift remains constant under various load conditions in the proposed control strategy. When the positions of the primary and secondary coils are fixed, the mutual inductance and coupling coefficient can be measured during the initialization state before the power transfer, and the inverter phase-shift angle will be available according to (34) at a specific position. Moreover, an additional control variable in X_1 should be available to tune the phase difference between the inverter voltage and inverter current via impedance matching under various load conditions and misalignment situations.

Based on the previous analysis, both X_1 and X_2 should be tunable to achieve optimal load matching, receiver network impedance matching, and soft switching of the inverter
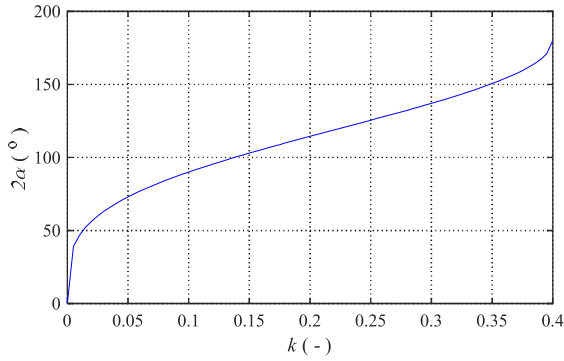
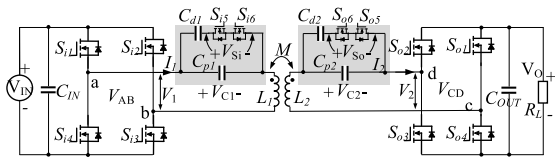**FIGURE 4.** Characteristics between phase-shift angle and *k*.

FIGURE 5. System circuit with the SCC.

FIGURE 6. Operating waveforms of the proposed control strategy.

switches. Therefore, SCC is applied to the resonant capacitor on both the transmitter and receiver sides. As shown in Fig. 5, the resonant capacitor C_1 is replaced by capacitor C_{p1}, capacitor C_{d1}, and a bidirectional switch including S_{i5} and S_{i6}. Similarly, the resonant capacitor C_2 on the receiver side is replaced by capacitor C_{p2}, capacitor C_{d2} and a bidirectional switch including S_{o5} and S_{o6}. The parallel configuration of the SCC is implemented to reduce the current through the bidirectional switch, since the coil current has two branches through C_{p1} and C_{d1} respectively when the bidirectional switch is ON. However, the bidirectional switch shares the same current with a coil in the series configuration of the SCC with C_{p1} when the bidirectional switch is ON, although the voltage rating of the bidirectional switch is reduced in case the bidirectional switch is OFF. The phase overlap angles of the bidirectional switches are respectively 2δ and 2ρ on the transmitter and receiver sides, respectively, as shown in Fig. 6. The resulting LC impedance in the transmitter and receiver can be derived as

$$X_1 = \omega_s L_1 - \frac{1}{\omega_S (C_1 + C_{d1} sin(\delta))} \tag{35}$$

$$X_2 = \omega_s L_2 - \frac{1}{\omega_S (C_2 + C_{d2} sin(\rho))}. \tag{36}$$

The steady-state operating waveforms of the proposed control strategy are presented in Fig. 6. On the transmitter side, the full-bridge inverter consists of four switches, S_{i1}, S_{i2}, S_{i3}, and S_{i4}, driven by gate signals gi1, gi2, gi3, and gi4, respectively. Gate signals gi1 and gi4 are complementary. Gate signals gi2 and gi3 are complementary, and gi1 leads gi2 by 2α, resulting in an inverter phase shift angle 2α. The fundamental harmonic component $\mathbf{V}_1$ of the inverter output voltage $\mathbf{V}_{AB}$ leads inverter output current $\mathbf{I}_1$ by θ. On the receiver side, the full-bridge active rectifier consists of four
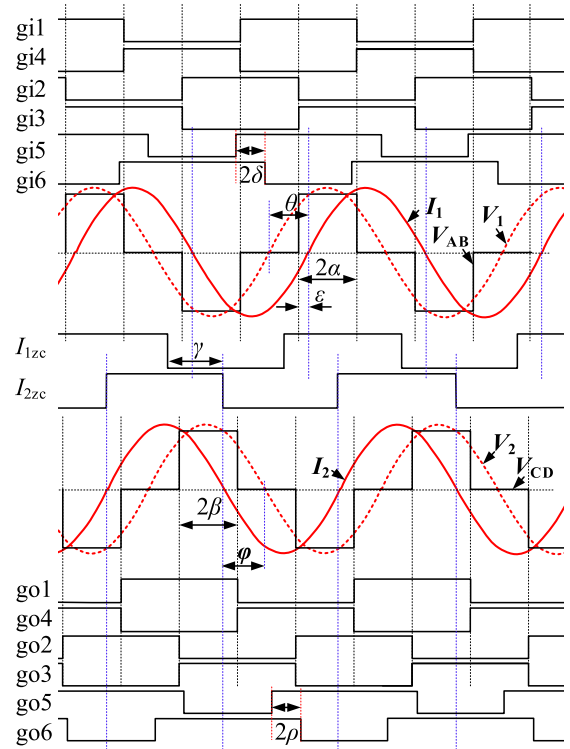
switches S_{o1}, S_{o2}, S_{o3}, and S_{o4}, controlled by gate signals go1, go2, go3, and go4, respectively. The gate signals go1 and go4 are complementary, whereas the gate signals go2 and go3 are complementary, and go2 leads go1 by 2β, resulting in the rectifier phase-shift angle 2β. The fundamental harmonic component $\mathbf{V}_2$ of the rectifier input voltage $\mathbf{V}_{CD}$ lags the rectifier input current $\mathbf{I}_2$ by φ. Switches S_{i5} and S_{i6} act as a bidirectional switch under the control of PWM driving signals gi5 and gi6, and the phase overlap angle is 2δ. Similarly, switches S_{o5} and S_{o6} act as bidirectional switch under the control of PWM driving signals go5 and go6, and their phase overlap angle is 2ρ. The operating principle of the SCC is described in detail in section III-A.

The proposed control strategy aims to achieve multi-objective optimization, such as power transfer efficiency, capability, distance, misalignment tolerance, passive component tolerance, and elimination of RTWFC. The optimal equivalent load resistance R_{eOPT} and receiver reactance matching criteria are derived by solving the derivatives of the efficiency formula. The rectifier phase-shift angle 2β is adjusted to regulate the output voltage, and the phase angle φ is adopted to match the rectifier resistance with the optimal load resistance for efficiency improvement. Thus, it can be solved according to (5) and (23) based on the estimation of the load resistance R_L and mutual inductance M,

$$\varphi = \pm acos\left(\frac{\pi}{sin(\beta)\sqrt{8}} \sqrt{\frac{1}{R_L} \sqrt{(\omega_s M)^2 \frac{R_2}{R_1} + R_2^2}} \right). \tag{37}$$

There exist two solutions for φ, however, to ensure soft-switching of rectifier switches, the rectifier current I_2 should lead to the falling edge of the rectifier voltage V_{CD}, meaning that I_2 always lies on the left of V_2 in Fig. 6 for optimal load matching. The active rectifier becomes capacitive. Thus, the value of φ is negative and the solution of φ becomes unique. In addition, the following criterion is always met for the optimal load matching:

$$cos(\varphi) \leq 1. \tag{38}$$

The control variable ρ can tune the impedance of the resonant capacitor on the receiver side, resulting in variable impedance X_2. The target X_2 is used to compensate for the impedance resulting from (6). Finally, the receiver network impedance becomes purely resistive, and the phase ρ is solved by combining (6), (22), and (37), as shown (39), at the bottom of the next page.

On the transmitter side, once the mutual inductance M is estimated, the inverter phase-shift angle 2α can be calculated using (34). The control variable δ is used to dynamically tune impedance X_1, resulting in soft switching of the inverter switches. The control variable δ can be derived by solving (16), (29), (33), and (35).

$$\delta = asin\left(\frac{1}{c_{d1}}\left(\frac{1}{\omega_s\left(\omega_s L1 - \frac{M_{max}}{\omega_s}\sqrt{\sqrt{x^3 - x^2}}\right)} - C1\right)\right). \tag{40}$$

In summary, the control of the transmitter and receiver sides is decoupled by the independent modulation of the control variables separately, resulting in the elimination of RTWFC. Therefore, control stability and reliability issues arising from the long propagation delay in real-time wireless communication can be addressed. The inverter phase-shift angle is adaptive to the variation in the magnetic coupling, and phase δ controls the impedance matching for soft-switching of inverter switches, which results in the regulation of power transfer. The rectifier phase-shift angle and the phase difference between the rectifier voltage and current are used to efficiently deliver the required output power, and phase ρ controls impedance matching to minimize the reactive power in the resonant receiver network. The disturbance of magnetic coupling from the distance variation and misalignments between coils is compensated by regulating the tunable resonant capacitors of the transmitter and receiver sides.

Although the control of the transmitter and receiver sides is decoupled with no RTWFC during the power transfer, the control variables affect each other. On the receiver side, the phase-shift angle 2β of the active rectifier is utilized to regulate the output voltage, while it changes the equivalent load resistance R_e according to (5); therefore, the phase difference between the rectifier voltage and current should be controlled to tune R_e to match the optimal load resistance in (23). In addition, the equivalent load reactance X_e in (6) is adjusted
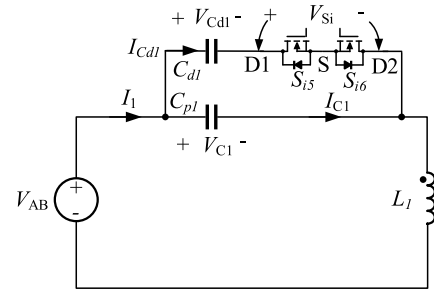

FIGURE 7. Circuit diagram of the PWM controlled capacitor.

by both the phase-shift angle 2β and the phase difference φ. The loop reactance in the receiver can be compensated, as in (22) and (36), by tuning the phase ρ in the variable resonant capacitor. Therefore, the control variables on the receiver side are coupled in the proposed control strategy. On the other hand, the inverter phase shift 2α and the coupling coefficient between coils are positively correlated. Thus, the inverter phase shift 2α is uniquely defined under specific magnetic coupling conditions and load independence. Moreover, (29) should be satisfied to maintain ZVS for inverter switches, where the phase difference θ between the inverter voltage and current is tuned by adjusting phase δ in the variable resonant capacitor according to (9), (15), (16), and (35).

III. IMPLEMENTATION OF THE PROPOSED CONTROL STRATEGY

As shown in Fig. 5, SCC is used to tune the effective impedance of the resonant capacitor dynamically and continuously. The circuit diagram and operation of the SCC are analyzed in detail. Moreover, control strategies are implemented on both the transmitter and receiver sides. Besides, the mutual inductance estimation method is adopted in the proposed control strategy for efficiency optimization.

A. OPERATION OF THE VARIABLE CAPACITOR
A circuit diagram of the SCC is shown in Fig. 7, and the operating waveforms are shown in Fig. 8. Two N-MOSFETs are connected in series to act as a bidirectional switch. A tuning capacitor C_{d1} is connected to the bidirectional switch in series, and both C_{d1} and the bidirectional switch are connected to the primary resonant capacitor C_{p1} in parallel. The resulting equivalent capacitance C_{1e} can be represented as

$$C_{1e} = f\left(C_{d1}, \delta\right) + C_{p1}. \tag{41}$$

The operating waveforms of the bidirectional switch are presented in Fig. 8, where the drain-source voltages for both switches are denoted as V_{D1S} and V_{D2S}, respectively. The drain-drain voltage of the bidirectional switch is denoted as V_{Si}, and dual MOSFETs are controlled by different PWM signals with a 180° phase shift. The waveform of V_{D1S} shows that switch S_{i5} is turned on and off at zero drain-source voltage, while the waveform of V_{D2S} shows that switch S_{i6} is turned on and off at zero drain-source voltage. The plot of V_{Si}
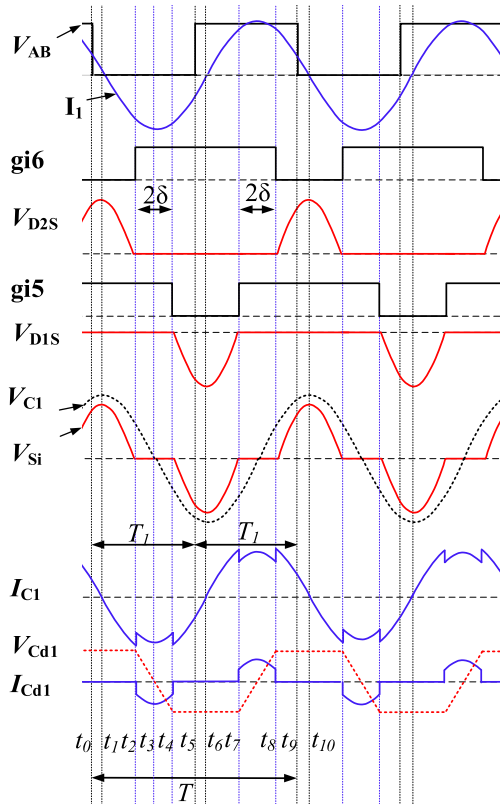
FIGURE 8. Operating waveform of the SCC.

is the sum of V_{D1S} and V_{D2S}. The condition that the middle of the OFF time of the PWM signal aligns with the zero-crossing point of $\mathbf{I}_1$ should be satisfied to ensure ZVS operation for both MOSFETs in the bidirectional switch. In addition, the ON duration of both PWM signals is $(\pi + 2\delta)$.

The equivalent capacitance of C_{d1} with a bidirectional switch can be calculated as follows:

$$C_{d1\ eq} = \frac{\Delta Q}{\Delta V_{Cd1\ eq}} \tag{42}$$

where ΔQ is the charge change in C_{d1} and ΔV_{Cd1eq} is the equivalent voltage change of C_{d1} during a quarter of T $(t_1 - t_3)$. Because the series-connected C_{d1} and the bidirectional switch are connected to C_{p1}, the equivalent voltage change over C_{d1} is equal to the voltage change over C_{p1}:

$$\Delta V_{Cd1\ eq} = V_{C1\ pk}. \tag{43}$$

The voltage over C_{d1} (V_{Cd1}) remains unchanged during $(t_1 - t_2)$. The voltage change of V_{Cd1} occurs during $(t_2 - t_3)$ and can be obtained as

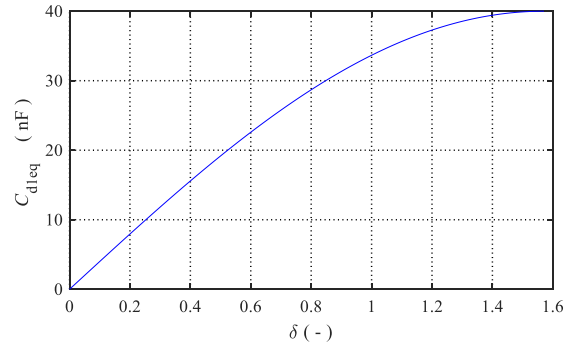$$\Delta V_{Cd1} = \frac{\Delta Q}{C_{d1}}. \tag{44}$$

FIGURE 9. Relationship between equivalent capacitance and control angle δ.

The voltage over C_{d1} at t_3 equals the voltage over C_{p1} since the bidirectional switch is turned ON under ZVS operation at the same time,

$$\Delta V_{Cd1} = V_{C1\ pk} sin(\delta). \tag{45}$$

Combining (42), (43), (44), and (45), the equivalent capacitance C_{d1eq} can be derived as

$$C_{d1\ eq} = C_{d1} sin(\delta). \tag{46}$$

The relationship between the equivalent capacitance over the PWM phase and duty cycle is shown in Fig. 9. (46) can be rewritten as,

$$C_{1e} = C_{d1} sin(\delta) + C_{p1}. \tag{47}$$

When the PWM signals are continuously ON, i.e., $\delta = \pi/2$, the equivalent resonant capacitance reaches its maximum value.

$$C_{1e\_max} = C_{p1} + C_{d1}. \tag{48}$$

When the PWM signals are always OFF, i.e., $\delta = 0$, C_{d1} is disconnected from the resonant network. Thus, the equivalent resonant capacitance reaches a minimum value,

$$C_{1e\_min} = C_{p1}, \tag{49}$$

the PWM phase δ is within the range,

$$0 \leq \delta \leq \frac{\pi}{2}. \tag{50}$$

B. TRANSMITTER SIDE CONTROL SCHEME
The transmitter-side control scheme is plotted in Fig. 10, and the control variables on the transmitter side are the phase-shift angle 2α and the PWM phase angle δ. The inverter phase-shift angle 2α is load-independent and corresponds only to the magnetic coupling condition between the transmitter and receiver coils. Then, the phase-shift angle 2α can be calculated by the phase-shift adaptation module according to (34), which generates four PWM driving signals for driving

$$\rho = asin\left(\frac{1}{C_{d2}}\left(\frac{1}{\frac{4}{\pi^2}\omega_S R_L sin\left(2acos\left(\frac{\pi}{sin(\beta)\sqrt{8}}\sqrt{\frac{\omega_S M}{R_L}}\right)\right) sin^2(\beta) + \omega_S^2 L_2} - C_2\right)\right). \tag{39}$$

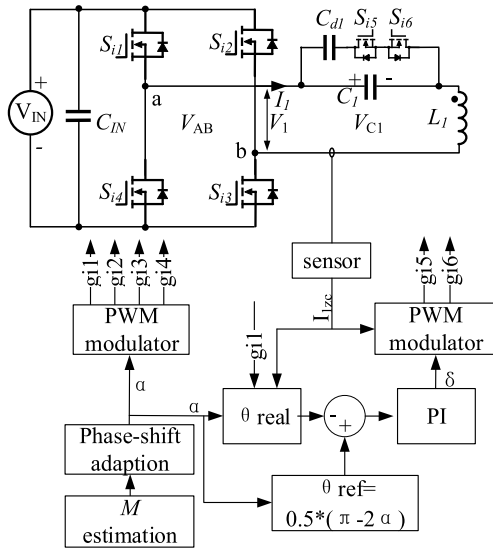**FIGURE 10.** The control scheme on the transmitter side.
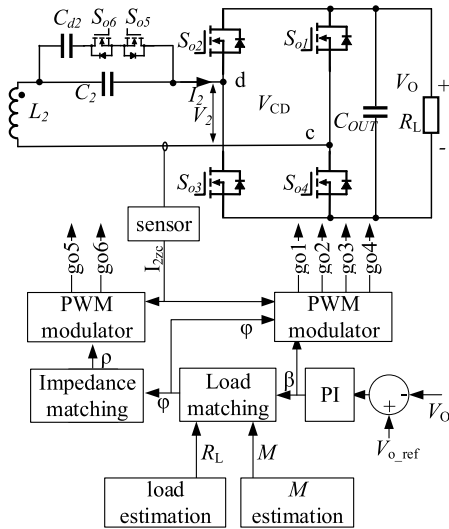

FIGURE 11. The control scheme on the receiver side.

inverter switches. The value θ is obtained by detecting the gate signal gi1 and the zero-crossing signal of the inverter current and combining the actual phase-shift angle 2α. The reference value θ_{ref} is $(\frac{\pi}{2} - \alpha)$, and the difference between the actual θ and θ_{ref} is fed to a proportional-integration (PI) controller. The PWM modulator generates PWM signals with a phase overlap of 2δ to drive the bidirectional switch in the SCC. Finally, impedance X_1 is tuned by the transmitter control loop for inverter's soft switching.

C. RECEIVER SIDE CONTROL SCHEME

The receiver-side control scheme is plotted in Fig. 11, and the control variables on the receiver side are the phase-shift angle 2β of the full-bridge rectifier, the phase difference φ between the rectifier voltage and current, and the PWM phase angle ρ of the bidirectional switch in the SCC. V_O is sensed
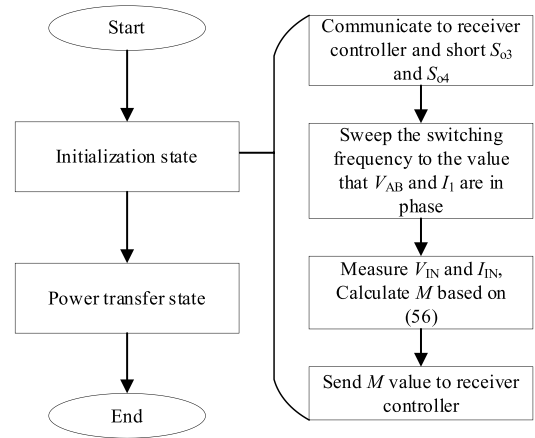

FIGURE 12. System workflow with *M* estimation procedure.

and compared to the reference, and a PI controller controls the difference by tuning the rectifier phase-shift angle. The load-matching block is implemented to match the equivalent load R_e to the optimal load R_{eOPT} for maximum efficiency, where the phase difference is calculated according to (37). The load resistance is calculated from the measured output voltage and current. The zero-crossing signal I_{2zc} of the rectifier current is obtained by measuring the resonant current of the receiver. The PWM modulator generates four PWM signals with a phase-shift angle of 2β and phase difference φ. The impedance-matching block tunes the impedance X_2 by modulating the PWM phase angle ρ to compensate for the rectifier reactance X_e, resulting in purely resistive impedance of the receiver network. Similarly, the PWM modulator generates PWM signals with a phase overlap of 2ρ to drive the bidirectional switch in the tunable resonant capacitor.

D. SYSTEM WORKFLOW AND ESTIMATION OF MUTUAL INDUCTANCE

Fig. 12 shows the system workflow and the estimation procedure for mutual inductance. The proposed control strategy eliminates RTWFC in the control loop of the output regulation during the power transfer state. There exists an initialization state before the power transfer, and both the transmitter and receiver can exchange information, including the mutual inductance M, via wireless communication in the initialization state. The mutual inductance is estimated in the initialization state, whereas the calculation of specific control variables is performed in the power-transfer state. Moreover, the control of the transmitter and receiver sides is decoupled by the independent modulation of the control variables separately. Therefore, the calculation burden is relatively acceptable, and the digital controller TI TMS320F28335 is adopted to implement the control strategy on both the transmitter and receiver.

Mutual inductance, which is one of the critical parameters required in the proposed control strategy, varies according to the change in the relative position between the transmitter and

the receiver coils. Therefore, it is necessary to estimate the mutual inductance to implement the proposed control strategy. A simple estimation algorithm combining the method in [23], [32] is formulated. The inverter output impedance can be calculated according to (9), (13), (14), (15), and (16):

$$\frac{V_1}{I_1}e^{j\theta} = R_1 + jX_1 + \frac{(\omega_S M)^2}{R_2 + R_e + j(X_2 + X_e)}. \quad (51)$$

Both resistance R_e and reactance X_e can be eliminated by shorting S_{o3} and S_{o4}. Besides, X_1 and X_2 can be eliminated by sweeping the switching frequency to the resonant frequency, resulting in a phase synchronization between V_{AB} and I_1. Therefore, the impedance in (51) can be simplified as

$$\frac{V_1}{I_1} = R_1 + \frac{(\omega_S M)^2}{R_2}. \quad (52)$$

Assuming the input power is equal to the inverter output power,

$$V_1 I_1 cos(\theta) = V_{IN} I_{IN}. \quad (53)$$

The inverter phase-shift angle is maximized by setting $\alpha = \frac{\pi}{2}$, and the inverter output voltage in (3) becomes

$$V_1 = \frac{2\sqrt{2}}{\pi} V_{IN}. \quad (54)$$

According to (52) and (53), (51) can be represented as

$$\frac{V_1}{I_1} = \frac{8}{\pi^2}\frac{V_{IN}}{I_{IN}} = R_1 + \frac{(\omega_S M)^2}{R_2}. \quad (55)$$

Therefore, the mutual inductance can be obtained by solving (55),

$$M = \frac{1}{\omega_s}\sqrt{\left(\frac{8}{\pi^2}\frac{V_{IN}}{I_{IN}} - R_1\right)R_2}. \quad (56)$$

The estimation of M follows the flowchart in Fig. 12. First, the transmitter communicates with the receiver to short S_{o3} and S_{o4}, both switches S_{i5} and S_{i6} are switched OFF in the initialization state, while switches S_{o5} and S_{o6} are driven by the switching signals with a phase ρ of 0.253 to generate the same capacitance of the secondary variable resonant capacitor with C_{1e}. Thus, both the primary and secondary networks can be tuned to an identical resonant frequency based on identical coil inductance. Then the resonant condition on the primary side is tuned by sweeping the switching frequency, and M is calculated according to (56). This measurement error causes a certain deviation in the calculated mutual inductance. Fig. 4 shows that the phase-shift angle varies slowly along with the specified k range of 0.2 to 0.3, and the ZVS of the inverter switches is maintained by the dynamically tuned resonant capacitor. Thus, the accuracy of the mutual inductance estimation has a minor influence on primary-side control. As shown in Fig. 11, the output voltage is regulated by adjusting the phase-shift angle, which is irrelevant to M estimation. However, the optimal load resistance is approximately proportional to the mutual inductance in systems with identical transmitter and receiver coils. Therefore, the effect
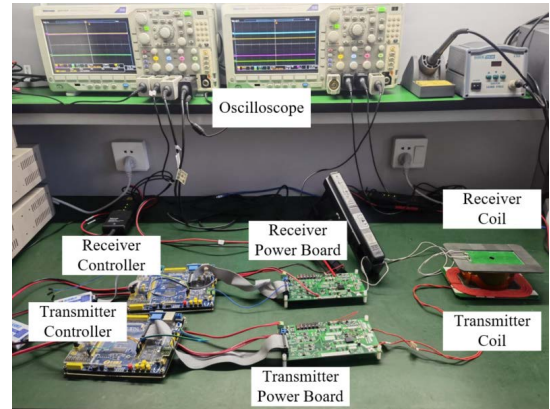

FIGURE 13. Experimental prototype.

of optimal load matching will be attenuated by low M estimation accuracy. The transmitter sends the calculated M to the receiver via wireless communication during the initialization state. Moreover, the receiver is static for wireless charging once it aligns with the transmitter coil, and M is not updated during power transfer. However, the method of online M estimation during power transfer can be further developed to enable WPT while the coils move.

IV. EXPERIMENTAL VERIFICATION

To verify the analysis of the proposed multivariable coordinated control strategy, an experimental prototype was built as shown in Fig. 13 to conduct experiments, and the parameters implemented in the experimental prototype are listed in Table 2. The proposed system is developed to wirelessly power cleanroom equipment with a constant voltage. The transmitter and receiver share identical hardware, including the controller board, power board, and coils. An off-the-shelf development board with a digital controller TI TMS320F28335 is adopted as the control board. The prototype is powered by a DC power source, the electronic load is used to simulate the load resistance, and the operating waveforms are captured using an MDO3024 oscilloscope.

A. MEASURED WAVEFORMS

The experimental waveforms of the inverter, rectifier, and tuning capacitor in the proposed system are shown in Fig. 14. V_{AB} is the inverter output voltage, I_1 is the inverter output current, V_{CD} is the rectifier input voltage, and I_2 is the rectifier input current. Moreover, gi5 and go5 are the gate-driving PWM signals for switches S_{i5} and S_{o5}, respectively. V_{So} is the drain-drain voltage of the bidirectional switch consisting of S_{o5} and S_{o6}. V_{Si} is the drain-drain voltage of the bidirectional switch consisting of S_{i5} and S_{i6}. The waveforms in the left column show the operation of the inverter and rectifier, and those in the right column show the operation of the SCCs.

Fig. 14 (a) and (b) are measured at full load and under the maximum coupling coefficient of 0.3, whereas Fig. 14 (c) and (d) show the results at a 67% load. The
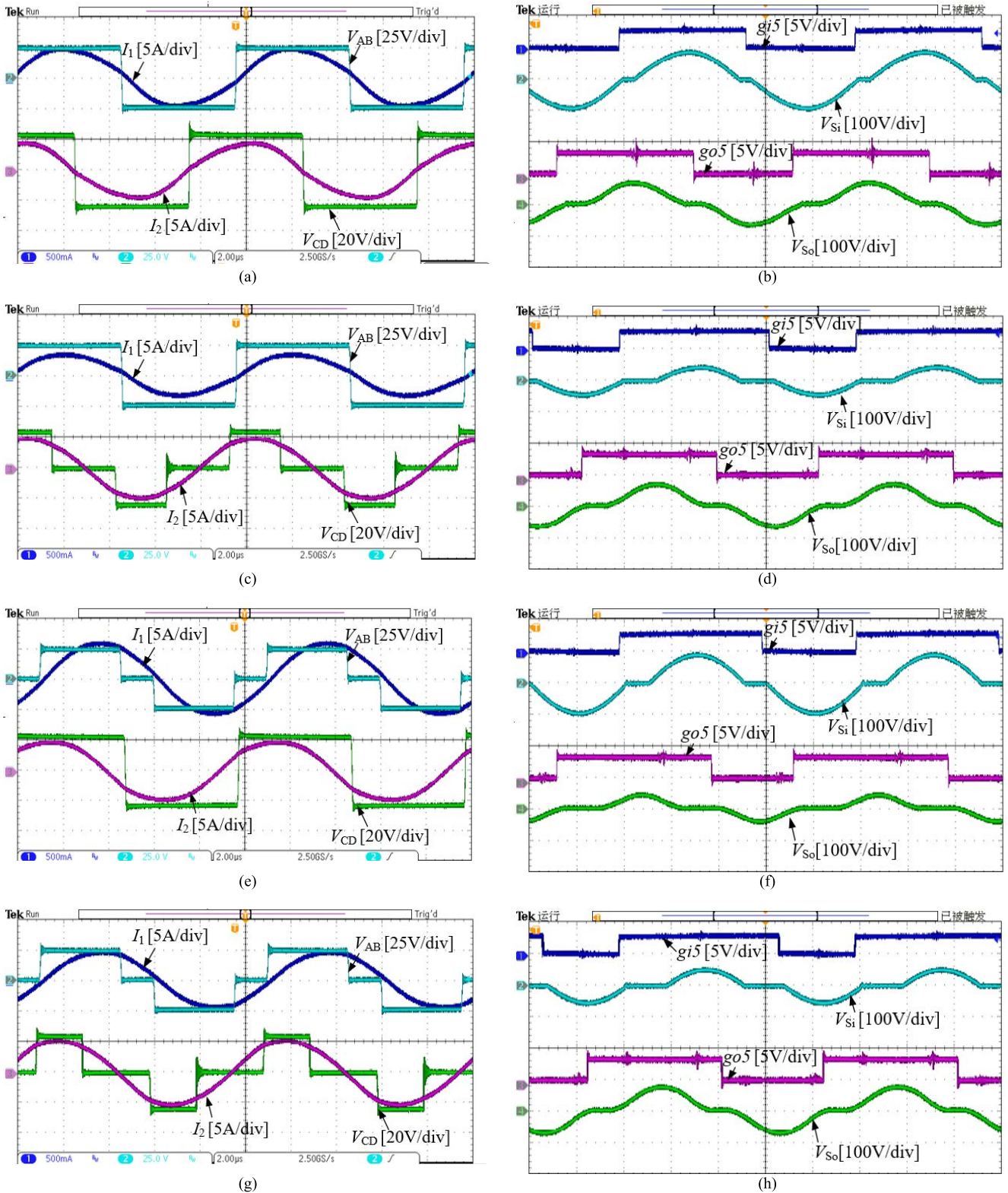
FIGURE 14. Experimental waveforms of inverter, rectifier, and tuning capacitor. Inverter voltage VAB, inverter current I_1, rectifier voltage V_{CD}, rectifier current I_2, S_{o5} gate-source voltage go5, S_{o5} and S_{o6} drain-drain voltage V_{So}, S_{i5} gate-source voltage gi5, S_{i5} and S_{i6} drain-drain voltage V_{Si}, (a) and (b) $k = 0.3$, $R_L = 8\ \Omega$, (c) and (d) $k = 0.3$, $R_L = 12\ \Omega$, (e) and (f) $k = 0.2$, $R_L = 8\ \Omega$, (g) and (h) $k = 0.2$, $R_L = 12\ \Omega$.

coupling coefficient is 0.3 when the distance between the transmitter coil and the receiver coil is 35 mm. The rectifier

input current I_2 leads to the rising edge of the rectifier input voltage V_{CD} for soft switching and optimal load matching.

TABLE 2. List of circuit parameters.

Parameters	Symbol	Value
Self-inductance of primary coil	L_1	36.09 μH
Self-inductance of secondary coil	L_2	36.09 μH
Coupling coefficient	k	0.2-0.3
Primary resonant capacitor	C_{p1}	70 nF
Secondary resonant capacitor	C_{p2}	60 nF
Primary tunable capacitor	C_{d1}	50 nF
Secondary tunable capacitor	C_{d2}	40 nF
Load resistance	R_L	8-16 Ω
Input DC voltage	V_{IN}	24 V
Rated output power	$P_{out.rated}$	72 W
Output DC voltage	V_O	24 V
Switching frequency	f_s	100 kHz
Bridge MOSFETs	S_{i1} -S_{i4}	BSC097N06NS
Tuning MOSFETs	S_{i5}-S_{i6}	BSC13DN30NS
Diode in the rectifier	-	V10P10-M3/86A

The loop reactance of the rectifier network is compensated by tuning the effective resonant capacitance via on-time control of switches S_{o5}, and S_{o6}. On the transmitter side, the phase-shift angle is maximized to π under the designed maximum mutual inductance. Theoretically, the inverter output current I_1 should align with the rising edge of the inverter output voltage V_{AB} for soft-switching. Nevertheless, owing to the existing parasitic capacitance and inductance, the exact control of the phase alignment is difficult. Therefore, the phase difference between the rising edge of V_{AB} and inverter output current is set to 10° for robust operation. When the output power decreases, the phase-shift angle of the inverter remains constant, as shown in Fig. 14 (a) and (c), as expected, and the phase-shift angle of the active rectifier is tuned by a PI controller to regulate the target output voltage, while the on-time of gi5 increases to regulate the phase difference between I_1 and V_{AB} for soft switching.

Fig. 14 (e) and (f) are measured at full load and under misalignment, whereas Fig. 14 (g) and (h) show the results at a 67% load. The coupling coefficient is 0.2 when the distance between the transmitter coil and the receiver coil is 48 mm. The inverter phase shift is reduced to 129° at this specific coupling coefficient. Moreover, the inverter output voltage V_{AB} still leads I_1 owing to the dynamic capacitance tuning in Fig. 14 (f). Meanwhile, I_2 leads V_{CD} for optimal load matching and soft switching, and the dynamic capacitance is tuned by go5 and go6 for reactance matching, resulting in a purely resistive receiver network. As shown in Fig. 14 (e) and (g), the inverter phase shift remains the same under reduced power; nevertheless, the rectifier phase shift is reduced to regulate the output voltage. Moreover, inverter switches always operate under soft-switching under the dynamic impedance compensation of capacitance tuning by gi5 and gi6. However, the rectifier switches are hard switching because I_2 and V_{CD} are in phase.

Note that a minimum phase-shift angle of the active rectifier exists for optimal load matching owing to (38),

$$\beta_{min} = asin\left(\frac{\pi}{\sqrt{8}}\sqrt{\frac{\omega_s M}{R_L}}\right). \quad (57)$$
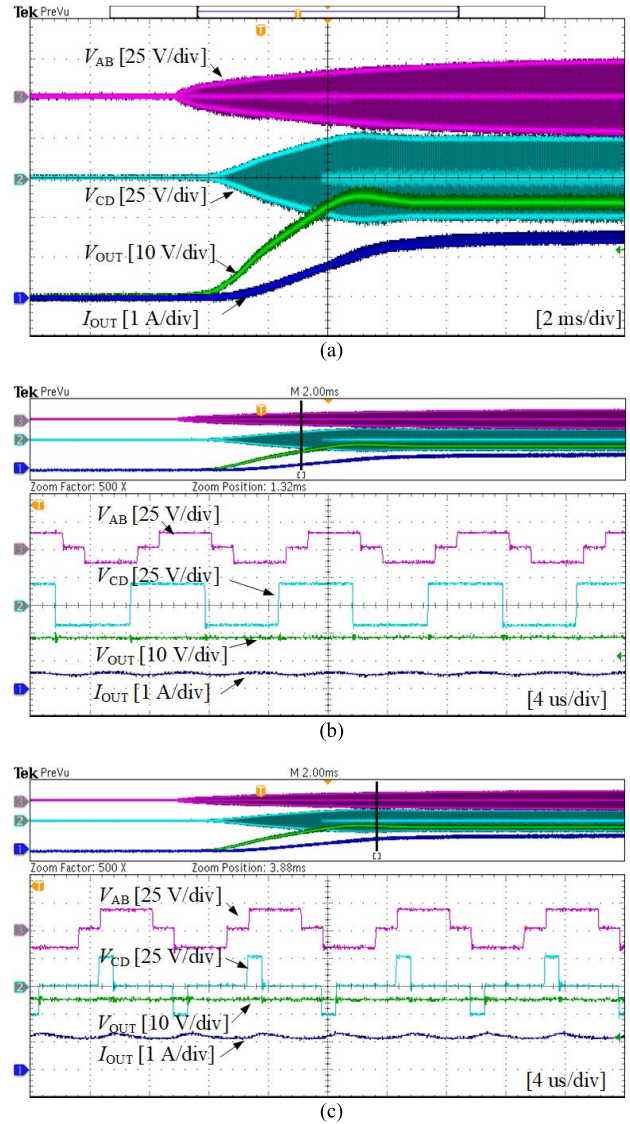

FIGURE 15. Experimental waveforms of the inverter, rectifier, output voltage and current at startup, (a) overview, (b) zoomed at 1.32 ms, (c) zoomed at 3.88 ms.

Therefore, the phase-shift angle 2β of the active rectifier decreases with increasing load resistance, and when β is smaller than β_{min}, optimal load matching is not achievable, as φ becomes purely imaginary. However, reactance compensation of the receiver network is still feasible by tuning the resonant capacitor and setting φ to zero. Optimal load matching is not achievable in Fig. 14 (c) and (g); thus, I_2 and V_{CD} are in phase. Therefore, hard switching occurs on the rectifier switches.

B. TRANSIENT RESPONSE AND SOFT-SWITCHING
The transient behaviors at the startup and load-step are studied under misalignment and are presented in Fig. 15 and Fig. 16, respectively. The waveforms of the output voltage show slight overshoot and undershoot in a short response time at the startup and load-step, respectively. Thus, the control
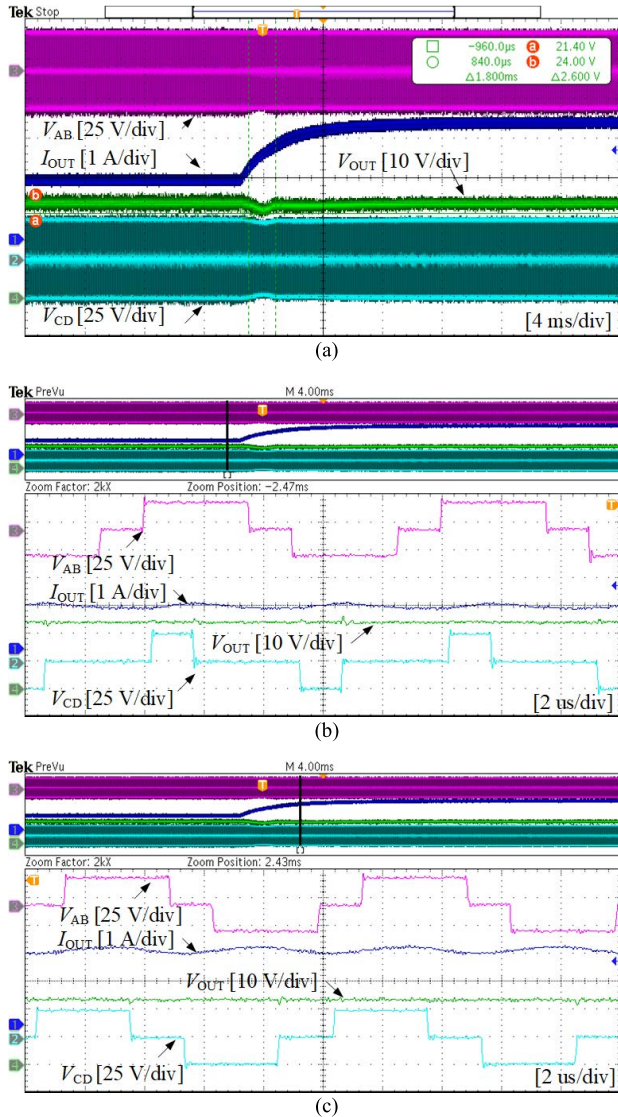
FIGURE 16. Experimental waveforms of the inverter, rectifier, output voltage, and current at load-step from 1.5 A to 3 A, (a) overview, (b) zoomed at −2.47 ms, (c) zoomed at 2.43 ms.

FIGURE 17. Measured dynamic response of the SCC.

FIGURE 18. Experimental waveforms of soft-switching operation, (a) inverter switch (b) rectifier switch (c) switch in the SCC.

loop of the output regulation is stable. The receiver phase shift is set to its maximum value π by default for a fast response at startup. Therefore, this initial beta value is $\pi/2$. As shown in Fig. 15, when the output voltage is close to the reference value, the PI controller regulates the output voltage by tuning the receiver phase shift to a proper value. The transient response of the current load-step I_{OUT} from 1.5 A to 3 A in Fig. 16 presents a 1.8 ms recovery time, which is much faster than that of 42 ms with RTWFC in [18].

The dynamic response of the SCC is measured with the δ values from 0.408 to 0.204 and plotted in Fig. 17, where the phase overlap between the driving signals gi5 and gi6 changes accordingly. Meanwhile, the amplitude of the drain-drain voltage V_{Si} increases quickly and the waveform of V_{Si} remains sinusoidal. Moreover, both driving signals of the SCC are synchronized to the zero-crossing signal of the
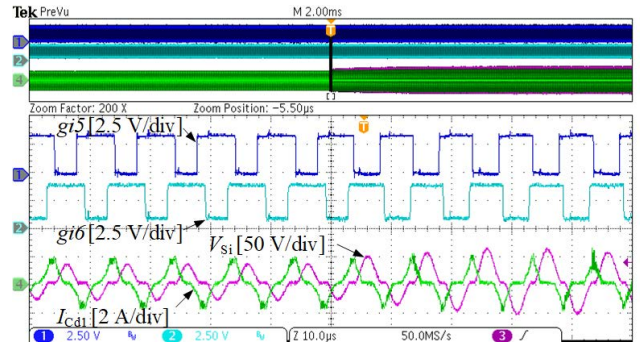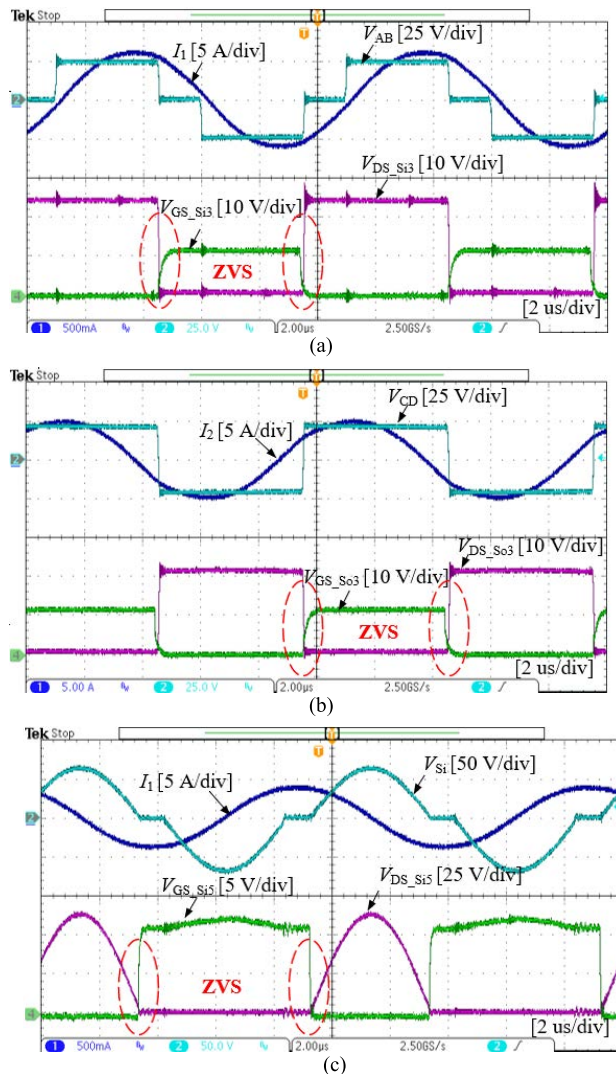
inverter current, as shown in Fig. 17, where no spike occurs on the current I_{Cd1} because soft-switching is realized in the switches of the SCC, even during the step disturbance.

The soft-switching operation of the switches in the inverter, rectifier, and resonant network was investigated.
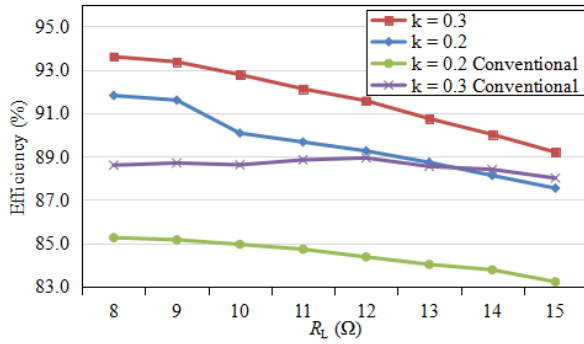
FIGURE 19. Measured power transfer efficiency under various load conditions and different coupling coefficients.

The experimental waveforms of the inverter switch S_{i3} drain-source voltage V_{DS_Si3}, gate-source voltage V_{GS_Si3}, inverter output voltage V_{AB}, and inverter output current I_1 are shown in Fig. 18(a). Under the control of dynamic capacitance tuning, the inverter output current I_1 lags the rising edge of the V_{AB}. Therefore, the bridge switches operate at soft switching. In the receiver, the experimental waveforms of rectifier switch S_{o3}, rectifier input voltage V_{CD}, and rectifier input current I_2 are shown in Fig. 18(b). To ensure soft switching of the rectifier switches, the rectifier current I_2 should lead to the falling edge of the rectifier voltage V_{CD}. In other words, the soft-switching condition for rectifier switches is $\varphi > \pi/2 - \beta$. It is observed that I_2 leads to V_{CD}, and switch S_{o3} operates at soft switching. However, when the load resistance increases and the mutual inductance decreases, the rectifier phase shift is reduced for output regulation, hard-switching occurs due to large phase-shift angle β and small phase difference φ. Therefore, the soft-switching region of the rectifier is narrow. Besides, the experimental waveforms of the inverter output current I_1, the drain-drain voltage V_{Si} of the bidirectional switch, drain-source voltage V_{DS_Si5}, and gate-source voltage V_{GS_Si5} are presented in Fig. 18(c). It is found that the drain-source voltage V_{DS_Si5} behaves sinusoidally during off-time, and the switch is turned on and off at ZVS.

C. MEASURED EFFICIENCY

Fig. 19 shows the comparison of the DC-DC efficiency between the proposed control strategy and the conventional voltage-tuning method under various load and coupling conditions. The DC-DC efficiency is obtained from the power analyzer PW6001 by measuring the voltage and current of both the DC input of the inverter and the DC output of the rectifier. The conventional voltage tuning method in [3] is implemented on the same prototype with identical circuit parameters but without a tunable capacitor and with a diode rectifier. The diode V10P10-M3/86A with a low forward voltage drop is selected in the experimental prototype. The specified power loss at 3 A is 1.6 W, which is considerably low for the comparison. In addition, both the primary resonant capacitor and secondary resonant capacitor are tuned in the resonant state at the switching frequency. The input voltage

of the inverter in the conventional voltage-tuning method is adjusted by a DC source to deliver the target output voltage under various load conditions. Because there is no dynamic tuning for the resonant capacitor in the conventional method, the resonant operation and reactance compensation cannot be guaranteed owing to the capacitor tolerance and inductance variations under different magnetic couplings. It is observed that the proposed multi-variable coordinated control strategy demonstrated a 5% higher efficiency owing to optimized load matching, reactance compensation, and soft-switching of the inverter and rectifier switches in the normal position. Furthermore, the power efficiency is improved to 93.6% under strong magnetic coupling at a 24 V output.

D. DISCUSSION

In this paper, optimal load matching is not achieved in a wide range. This is because the equivalent load resistance R_e depends on the rectifier phase-shift angle 2β, the phase difference φ between the rectifier voltage and current, and the load resistance R_L according to (5). Since β is adjusted to regulate the output voltage in the proposed control strategy as shown in (24), only the phase angle φ is adopted to match R_e with R_{eOPT} for the optimal load matching. Moreover, the equivalent load resistance R_{eOPT} varies with the mutual inductance according to (23). Hence, the achievable range of the optimal load matching is narrow due to the limitation of the output regulation from β. A minimum phase-shift angle 2β of the active rectifier exists for the optimal load matching according to (57). 2β decreases with the increasing load resistance and when β decreases to a value smaller than β_{min}, the optimal load matching is not achievable, as φ becomes purely imaginary. As shown in Fig. 14(c) and 14(g), β is reduced for the output regulation in light load conditions (e.g., $R_L = 12\ \Omega$), and is smaller than β_{min}. Therefore, the optimal load matching becomes invalid, and the measured efficiency drops in Fig. 19.

On the other hand, the optimal load matching in the proposed control strategy remains valid for both different load resistance and magnetic coupling conditions if the real solution of (37) exists. This is because the phase difference φ between the rectifier voltage and current is adjustable in (5). The resulted R_e with different R_L and M can still be tuned by adjusting φ to match R_{eOPT}. As shown in Fig. 14(a) and 14(e), the optimal load matching is achieved at full load when k is 0.3 and 0.2. Moreover, for a given M, the optimal load matching can still be realized for various load resistance by tuning φ once the resulted β is smaller than β_{min}. Thus, the optimal load matching keeps feasible under heavy load conditions, not only in the rated R_L. Moreover, the efficiency optimization in heavy loads helps the system design in terms of cooling and volume.

V. CONCLUSION

This paper presents a multivariable coordinated control strategy for an SS-compensated DAB WPT converter to optimize efficiency and eliminate RTWFC. The output voltage

is regulated by tuning the phase-shift angle of the active rectifier. The SCC is used in the resonant capacitors for both the transmitter and receiver to implement continuously varying capacitance. The reactance in the receiver network is compensated by tuning the receiver resonant capacitor. The phase shift of the inverter is load-independent but adjusted to deal with various magnetic coupling conditions. A prototype operating at a constant frequency is implemented to verify the feasibility of the proposed control strategy. The optimal load matching is proven with a higher efficiency in heavy loads by adjusting the phase difference between the rectifier input voltage and current. The soft switching of inverter switches is guaranteed by the modulation of the SCC in the transmitter. Moreover, both switches in the SCC operate in soft switching. Compared with conventional voltage tuning, the proposed system demonstrates a 5% higher efficiency under normal conditions and a much faster transient response.

REFERENCES

[1] Z. Zhang, H. Pang, A. Georgiadis, and C. Cecati, "Wireless power transfer-an overview," *IEEE Trans. Ind. Electron.*, vol. 66, no. 2, pp. 1044–1058, Feb. 2019.

[2] M. Lu and K. Ngo, "Systematic design of coils in series–series inductive power transfer for power transferability and efficiency," *IEEE Trans. Power Electron.*, vol. 33, no. 4, pp. 3333–3345, Apr. 2018.

[3] Y. Zhang, T. Kan, Z. Yan, and C. C. Mi, "Frequency and voltage tuning of series–series compensated wireless power transfer system to sustain rated power under various conditions," *IEEE J. Emerg. Sel. Topics Power Electron.*, vol. 7, no. 2, pp. 1311–1317, Jun. 2019.

[4] X. Liu, T. Wang, X. Yang, N. Jin, and H. Tang, "Analysis and design of a wireless power transfer system with dual active bridges," *Energies*, vol. 10, no. 10, p. 1588, Oct. 2017.

[5] I. Iam, I. U. Hoi, Z. Huang, C. Gong, C.-S. Lam, and P.-I. Mak, "Constant-frequency and non-communication-based inductive power transfer converter for battery charging," *IEEE J. Emerg. Sel. Topics Power Electron.*, vol. 10, no. 2, pp. 2147–2162, Apr. 2022, doi: 10.1109/JESTPE.2020.3004259.

[6] Y. H. Sohn, B. H. Choi, E. S. Lee, G. C. Lim, G. H. Cho, and C. T. Rim, "General unified analyses of two-capacitor inductive power transfer systems: Equivalence of current-source SS and SP compensations," *IEEE Trans. Power Electron.*, vol. 30, no. 11, pp. 6030–6045, Nov. 2015.

[7] C. Zheng, J. S. Lai, R. Chen, and W. E. Faraci, "High-efficiency contactless power transfer system for electric vehicle battery charging application," *IEEE J. Emerg. Sel. Topics Power Electron.*, vol. 3, no. 1, pp. 65–74, Mar. 2015.

[8] H. H. Wu, A. Gilchrist, K. D. Sealy, and D. Bronson, "A high efficiency 5 kW inductive charger for EVs using dual side control," *IEEE Trans. Ind. Informat.*, vol. 8, no. 3, pp. 585–595, Aug. 2012.

[9] J. Lu, G. Zhu, D. Lin, Y. Zhang, H. Wang, and C. C. Mi, "Realizing constant current and constant voltage outputs and input zero phase angle of wireless power transfer systems with minimum component counts," *IEEE Trans. Intell. Transp. Syst.*, vol. 22, no. 1, pp. 600–610, Jan. 2021.

[10] X. Wang, J. Xu, H. Ma, and P. Yang, "A high efficiency LCC-S compensated WPT system with dual decoupled receive coils and cascaded PWM regulator," *IEEE Trans. Circuits Syst. II, Exp. Briefs*, vol. 67, no. 12, pp. 3142–3146, Dec. 2020.

[11] Z. Yan, Y. Zhang, K. Zhang, B. Song, S. Li, T. Kan, and C. C. Mi, "Fault-tolerant wireless power transfer system with a dual-coupled LCC-S topology," *IEEE Trans. Veh. Technol.*, vol. 68, no. 12, pp. 11838–11846, Dec. 2019.

[12] S. Li, W. Li, J. Deng, T. D. Nguyen, and C. C. Mi, "A double-sided LCC compensation network and its tuning method for wireless power transfer," *IEEE Trans. Veh. Technol.*, vol. 64, no. 6, pp. 2261–2273, Jun. 2015.

[13] X. Qu, Y. Jing, H. Han, S.-C. Wong, and C. K. Tse, "Higher order compensation for inductive-power-transfer converters with constant-voltage or constant-current output combating transformer parameter constraints," *IEEE Trans. Power Electron.*, vol. 32, no. 1, pp. 394–405, Jan. 2017.

[14] X. Qu, H. Han, S.-C. Wong, C. K. Tse, and W. Chen, "Hybrid IPT topologies with constant current or constant voltage output for battery charging applications," *IEEE Trans. Power Electron.*, vol. 30, no. 11, pp. 6329–6337, Nov. 2015.

[15] U. D. Kavimandan, S. M. Mahajan, and C. W. Van Neste, "Analysis and demonstration of a dynamic ZVS angle control using a tuning capacitor in a wireless power transfer system," *IEEE J. Emerg. Sel. Topics Power Electron.*, vol. 9, no. 2, pp. 1876–1890, Apr. 2021, doi: 10.1109/JESTPE.2020.2997822.

[16] H. Shui, D. Yu, S. Yu, H. H. C. Iu, T. Fernando, and H. Cheng, "An autonomous impedance adaptation strategy for wireless power transfer system using phase-controlled switched capacitors," *IEEE J. Emerg. Sel. Topics Power Electron.*, vol. 9, no. 2, pp. 2303–2316, Apr. 2021, doi: 10.1109/JESTPE.2019.2960878.

[17] D. Kim and D. Ahn, "Self-tuning LCC inverter using PWM-controlled switched capacitor for inductive wireless power transfer," *IEEE Trans. Ind. Electron.*, vol. 66, no. 5, pp. 3983–3992, May 2019.

[18] X. Wang, J. Xu, M. Leng, H. Ma, and S. He, "A hybrid control strategy of LCC-S compensated WPT system for wide output voltage and ZVS range with minimized reactive current," *IEEE Trans. Ind. Electron.*, vol. 68, no. 9, pp. 7908–7920, Sep. 2021, doi: 10.1109/TIE.2020.3013788.

[19] Y. Chen, H. Zhang, S.-J. Park, and D.-H. Kim, "A switching hybrid LCC-S compensation topology for constant current/voltage EV wireless charging," *IEEE Access*, vol. 7, pp. 133924–133935, 2019.

[20] Y. Li, W. H. Dong, Q. X. Yang, J. T. Zhao, L. Liu, and S. J. Feng, "An automatic impedance matching method based on the feedforward-backpropagation neural network for a WPT system," *IEEE Trans. Ind. Electron.*, vol. 66, no. 5, pp. 3963–3972, May 2019.

[21] J. Zhao, J. Zhang, and Y. Zhu, "A flexible wireless power transfer system with switch controlled capacitor," *IEEE Access*, vol. 7, pp. 106873–106881, 2019.

[22] B. Cheng and L. He, "Realize load-independent output with soft switching based on switched capacitor for wireless charger system," *IEEE Access*, vol. 10, pp. 10094–10104, 2022.

[23] J. Zhang, J. Zhao, Y. Zhang, and F. Deng, "A wireless power transfer system with dual switch-controlled capacitors for efficiency optimization," *IEEE Trans. Power Electron.*, vol. 35, no. 6, pp. 6091–6101, Jun. 2020.

[24] H. Zhu, B. Zhang, and L. Wu, "Output power stabilization for wireless power transfer system employing primary-side-only control," *IEEE Access*, vol. 8, pp. 63735–63747, 2020.

[25] K. Li, H. Yuan, S.-C. Tan, and S. Yuen Ron Hui, "Overshoot damping and dynamics improvement in wireless power transfer systems via receiver-side controller design," *IEEE Trans. Power Electron.*, vol. 37, no. 2, pp. 2362–2371, Feb. 2022.

[26] K. Song, R. Wei, G. Yang, H. Zhang, Z. Li, X. Huang, J. Jiang, C. Zhu, and Z. Du, "Constant current charging and maximum system efficiency tracking for wireless charging systems employing dual-side control," *IEEE Trans. Ind. Appl.*, vol. 56, no. 1, pp. 622–634, Jan. 2020.

[27] S. Chen, H. Li, and Y. Tang, "Extending the operating region of inductive power transfer systems through dual-side cooperative control," *IEEE Trans. Ind. Electron.*, vol. 67, no. 11, pp. 9302–9312, Nov. 2020.

[28] H.-C. Hsieh, A. D. Nguyen, and J.-S. Lai, "Output regulation with integrated SR switch duty cycle control for wireless power transfer systems," *IEEE J. Emerg. Sel. Topics Power Electron.*, early access, Sep. 22, 2021, doi: 10.1109/JESTPE.2021.3114359.

[29] W. Zhong and S. Y. R. Hui, "Charging time control of wireless power transfer systems without using mutual coupling information and wireless communication system," *IEEE Trans. Ind. Electron.*, vol. 64, no. 1, pp. 228–235, Jan. 2017.

[30] Z. Li, H. Liu, Y. Tian, and Y. Liu, "Constant current/voltage charging for primary-side controlled wireless charging system without using dual-side communication," *IEEE Trans. Power Electron.*, vol. 36, no. 12, pp. 13562–13577, Dec. 2021.

[31] L. Wu, B. Zhang, and Y. Jiang, "Position-independent CC/CV wireless EV charging system without dual-side communication and DC-DC converter," *IEEE Trans. Ind. Electron.*, vol. 69, no. 8, pp. 7930–7939, Aug. 2022, doi: 10.1109/TIE.2021.3108702.

[32] Y. Liu, U. K. Madawala, R. Mai, and Z. He, "Primary-side parameter estimation method for bidirectional inductive power transfer systems," *IEEE Trans. Power Electron.*, vol. 36, no. 1, pp. 68–72, Jan. 2021.
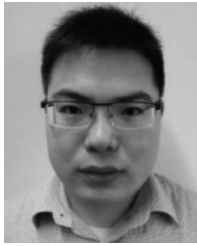
JIANTING LI (Member, IEEE) received the M.Sc. degree *(cum laude)* in electrical engineering from the Eindhoven University of Technology, Eindhoven, The Netherlands, in 2016. He is currently pursuing the Ph.D. degree with the Army Engineering University of PLA, Nanjing, China.

His research interests include switching topologies, wireless power transfer, high-frequency power conversion, and magnetics design.

JIANKE LI received the B.Sc. degree in control engineering from the Nanjing University of Aeronautics and Astronautics, Nanjing, China, in 2009, and the M.Sc. and Ph.D. degrees in electrical engineering from the PLA University of Science and Technology, Nanjing, in 2012 and 2015, respectively. He is currently a Lecturer at the Army Engineering University of PLA, Nanjing. His main research interests include distributed generation and wireless power transfer.

JINQUAN WANG received the B.Sc., M.Sc., and Ph.D. degrees in electrical engineering from the PLA University of Science and Technology, Nanjing, China, in 1983, 1989, and 2005, respectively. He is currently a Professor at the Army Engineering University of PLA. His main research interests include power distribution systems, power system protection, wireless power transfer, and distributed generation.

JINGJING CHEN received the B.Sc. degree in automation engineering from Nanjing Agriculture University, Nanjing, China, in 2006, and the M.Sc. degree in electrical engineering from the PLA University of Science and Technology, Nanjing, in 2009. She is currently a Lecturer at the Army Engineering University of PLA. Her main research interests include load characteristic analysis and distributed microgrid.

● ● ●